Gravity Effects on Steady Two-Dimensional Partially Premixed Methane–Air Flames

ZHUANG SHU, CHUN W. CHOI, SURESH K. AGGARWAL, VISWANATH R. KATTA,[†] and ISHWAR K. PURI*

Department of Mechanical Engineering, University of Illinois at Chicago, Chicago, IL 60607-7022

Under normal-gravity conditions the flame heat release produces both flow dilatation and buoyancy effects. While it may be possible to minimize gravitational effects in a fully premixed flame by isolating buoyancy effects to the lower-density postflame region or plume, this cannot be accomplished in nonpremixed flames. It is known that partially premixed flames can contain two reaction zones, one with a premixed-like structure and the other consisting of a transport-limited nonpremixed zone (in which mixing and entrainment effects are significant). For these reasons it is important to understand the fundamental interaction between flow dilatation and buoyancy effects in partially premixed flames. A detailed numerical study is conducted to characterize the effect of buoyancy on the structure of two-dimensional partially premixed methane–air flames. The computational model is validated by comparison with the experimentally obtained chemiluminescent emission from excited-C_2^* free radical species as well as with velocity vectors obtained using particle image velocimetry. Both the experiments and simulations indicate the presence of two reaction zones that are synergistically coupled, with each region providing heat and/or chemical species for the other. While the inner premixed flame is only weakly affected by gravity, the outer flame shows significant spatial differences for the two cases due to buoyancy-induced entrainment, since advection of air into the outer reaction zone increases in the presence of gravity. The presence of gravity induces more compact flames, influences the velocity profiles in the post–inner flame region, and increases the normal strain rate. Although the spatial differences between the 0- and 1-g flames are more significant on the lean side, the state relationships in that region are relatively unaffected by gravity. On the other hand, the inner (rich-side) reaction zone shifts toward less-rich locations in the presence of gravity, possibly due to the enhanced buoyant mixing. The 1-g flames exhibit a larger energy loss in the form of CO and H_2 emissions.   © 1999 by The Combustion Institute

INTRODUCTION

Partially premixed flames may be established by design by placing a fuel-rich mixture in contact with a fuel-lean mixture, but these flames also occur otherwise in many practical systems. For instance, initially nonpremixed combustion may involve regions of local extinction followed by partial premixing and reignition [1]. Likewise, partial premixing is an important process in nonpremixed flame liftoff phenomena, since the reactants can mix slightly prior to ignition [2, 3]. Nonuniform evaporation in spray flames can also result in local fuel-rich regions in which burning occurs in the partially premixed mode and the technique of lean direct injection used to achieve stable combustion and reduced pollutant levels involves regions of partially premixed combustion. In addition, unwanted fires can originate in a partially premixed mode when a pyrolyzed or evaporated fuel forms an initial fuel-rich mixture with the ambient air.

Under normal-gravity conditions the flame heat release produces both flow dilatation and buoyancy effects in partially premixed flames. Gas expansion due to the heating causes downstream motion normal to the flamefront. The buoyant gases accelerate the flow in an opposite direction to the gravity vector, causing air entrainment that enhances the fuel–air mixing and, consequently, influences the upstream region. While it is possible to minimize gravitational effects in a premixed flame by isolating buoyancy effects to the lower-density postflame region or plume, it is not so straightforward to do so in nonpremixed flames. Several investigations have established that partially premixed flames can contain two reaction zones [4–11], one with a premixed-like structure and the other consisting of a transport-limited nonpremixed zone (in which mixing and entrainment effects are significant). The thickness of the preheat zone associated with the premixed flame can be decreased by increasing the fuel–air equivalence ratio [12].
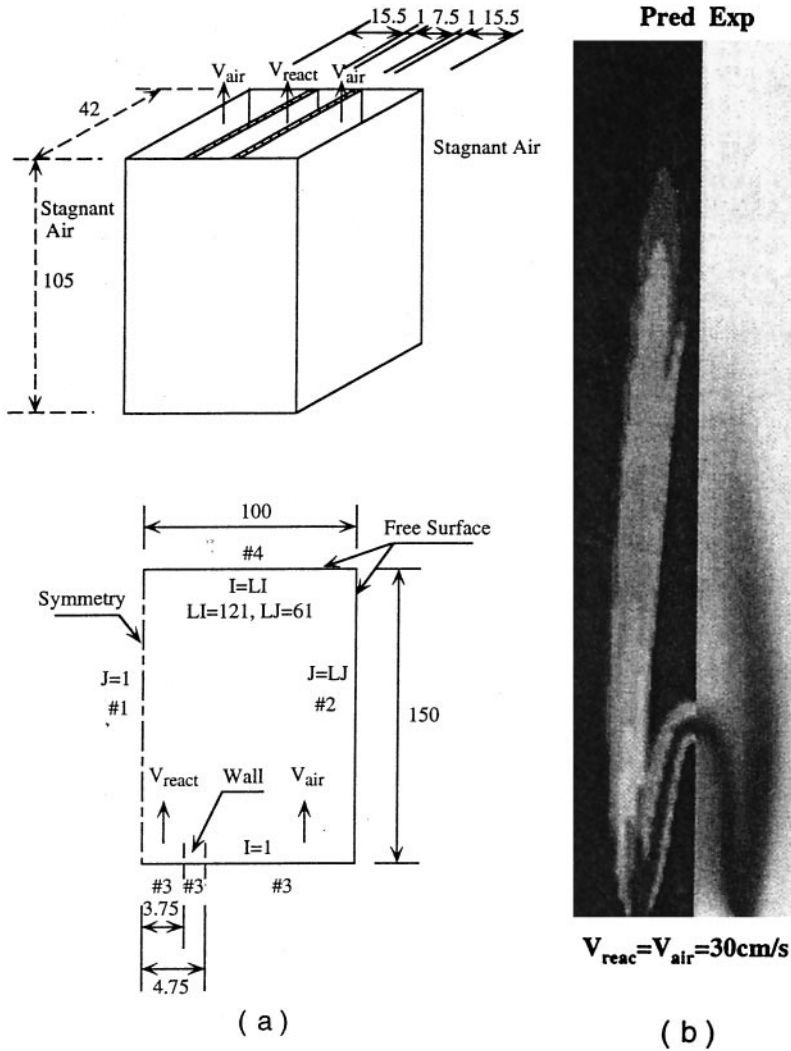
Fig. 1. (a) Schematic diagram of the 100 mm × 150 mm (or 61 × 121 gridline) computational domain. The symbols I and J, respectively, represent the axial and transverse gridlines. The boundary conditions are also specified. The simulated burner consists of an inner 7.5-mm slot with two 15.5-mm outer slots on either side of it. The wall thickness separating the slots is 1 mm. (b) Comparison of the simulated heat release rates with an experimentally obtained C_2-chemiluminescence image for a 1-g flame established at $\phi = 2$, and $V_{reac} = V_{air} = 30$ cm s^{-1}.

For these reasons it is important to understand the interaction between flow dilatation and buoyancy effects in partially premixed flames. This investigation compares the results obtained from numerical computations of two-dimensional, partially premixed methane–air flames established under both normal and zero-gravity conditions.

PROCEDURE

The computational study employs a flow configuration based on a rectangular Wolfhard-Parker slot burner that is schematically depicted in Fig. 1a and described elsewhere [13]. A fuel-rich mixture is introduced from the inner slot, and air from either side of it. Identical two-dimensional flames are established on either side of the centerline. The numerical simulations are conducted on one side of the symmetry plane (plane 1). The other three planes bounding the domain are the free surface (plane 2), the inflow boundary (plane 3), and the outflow boundary (plane 4).

The combustion process is simulated by em-

ploying a detailed numerical model based on the solution of time-dependent governing equations for a two-dimensional reacting flow. Using Cartesian coordinates (x, y), these equations can be written in the form

$$\frac{\partial(\rho\phi)}{\partial t} + \frac{\partial(\rho u\phi)}{\partial x} + \frac{\partial(\rho v\phi)}{\partial y}$$

$$= \frac{\partial}{\partial x}\left(\Gamma^{\phi}\frac{\partial\phi}{\partial x}\right) + \frac{\partial}{\partial y}\left(\Gamma^{\phi}\frac{\partial\phi}{\partial y}\right) + S^{\phi}$$

where ρ denotes density, and u and v the transverse (x) and axial (y) velocity components, respectively. The general form of the equation represents either of the mass, momentum, species, or energy conservation equations, depending on the variable used for ϕ. The transport coefficient Γ^{ϕ} and the source terms S^{ϕ} appearing in the governing equations are provided in Table 1 of Ref. 10. The set of governing equations is completed by using the overall species conservation equation and the equation of state $p = \rho R_u T \sum_i Y_i/M_i$, where R_u is the universal gas constant, T the temperature, and M_i the molecular weight of the ith species. The thermodynamic and transport properties appearing in the above equations are considered to be temperature- and species-dependent. First, the viscosity and thermal conductivity of the individual species are estimated based on Chapman-Enskog collision theory, following which those of the mixture are determined using the Wilke semi-empirical formulae. Chapman-Enskog theory and the Lennard-Jones potentials are used to estimate the binary-diffusion coefficient between each species and nitrogen D_{i-N_2}. The enthalpy h and specific heat are calculated for each species using the polynomial curve fits from Ref. 14.

An implicit algorithm is employed to solve the unsteady gas-phase equations. The governing equations are integrated by using a finite control volume approach with a staggered, non-uniform grid system. The finite-difference forms of the momentum equations are obtained using an implicit scheme [15], whereas those of the species and energy equations are obtained using a hybrid scheme [16]. Grid lines are clustered near the flame surfaces to resolve the steep gradients of the dependent variables. Bound-aries of the computational domain are shifted sufficiently to minimize the propagation of disturbances. An iterative Alternating Direction Implicit (ADI) technique is used for solving the resulting $(N_S + 3)$ sets of algebraic equations. A stable numerical-integration procedure is achieved by coupling the species and energy equations through the chemical-reaction source terms. At each time step the pressure field is calculated by solving the pressure Poisson equations at all grid points simultaneously and utilizing the Lower and Upper (LU) matrix-decomposition technique. Further details about the numerical procedure and the treatment of boundary conditions are provided in earlier publications [10, 11, 17–20]. Numerical validation studies employing different grids as well as comparison with experimental results are contained in Refs. 10, 11, and 13. A relatively detailed 17-species, 52-step C_1-mechanism is used to represent the CH_4–air chemistry [21].

The simulations are validated by comparing the predicted heat release profile with the experimentally obtained chemiluminescent emission due to excited-C_2^* free radical species from a representative flame established under normal-gravity conditions (cf. Fig. 1b). Images of the (1, 0) C_2 Swan band (at a wavelength of 473 nm [22]) are obtained using an ITT F4577 intensified 513×480 pixel camera through a narrow wavelength interference filter (470 ± 10 nm), and transferred to a frame grabber and processed by subtracting a representative background image. The emission can be interpreted as a signature of chemical reaction and heat release [23–26], since the excited C_2^* free radical species is short-lived, a good indicator of the reaction zone [25], and its light intensity is known to vary linearly with the volumetric heat release [13, 26]. The chemiluminescence images are directly proportional to the C_2^* formation rate and, thus, serve as a qualitative rate measure of the flame chemistry [27].

The computed velocity field is compared with velocity vectors obtained using particle image velocimetry (PIV) (cf. Fig. 2). The flow is seeded with TiO_2 particles and the particle illumination source consists of a double-pulsed Continuum Nd:YAG laser. Particle images are captured two times (due to the double pulse) using a TI RS-170 CCD camera. The digitized
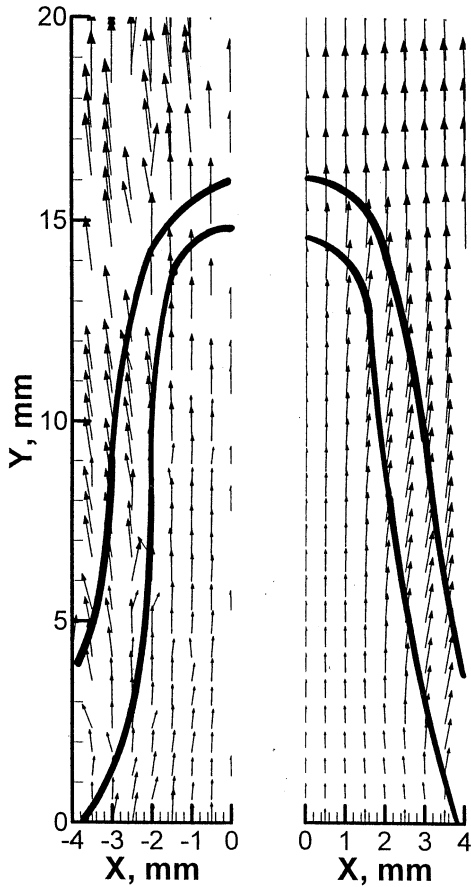
Fig. 2. Comparison of the measured ($-4 \leq x \leq 0$ mm) and predicted velocity vectors ($0 \leq x \leq 4$ mm) for a flame established at $\phi = 2$, $V_{air} = 30$ cm s^{-1}, and $V_{reac} = 30$ cm s^{-1}. The corresponding flame interface (chemiluminescent image and simulated heat release) is superimposed on the two plots.

image is fed to an array processor and analyzed using commercial autocorrelation software (TSI). Several precautions are taken to ensure reliability. Each interrogation spot contains more than 10 particle image pairs. Through extensive trial and error, the interrogation spot size is made small enough for a single vector to describe the flow at that location, and the laser sheet thick enough for out-of-plane particle motion to not be problematic and for sufficient particle pairs to be present. The particle displacement is kept greater than two particle image diameters, but not more than one-quarter of the interrogation spot size. The overlap between spots is adjusted to increase the vector density. In order to obtain accurate data for the

range of flow velocities, the PIV measurement window was set at 7.5×5.5 mm, respectively, in the x- and y-wise directions. This choice restricted the lowest possible velocity measurement for the acquired particle displacements to 30 cm s^{-1}. Further details of the PIV system are contained in Ref. 13.

RESULTS AND DISCUSSION

Figure 1b contains a comparison between the predicted heat release rate and the experimentally obtained emission image for a representative 1-g methane–air flame established at an equivalence ratio $\phi = 2$, and air and reactant velocities (respectively, V_{air} and V_{reac}) of 30 cm s^{-1}. Both the simulated heat release and the C_2^* emission signal are confined to two relatively thin sheet-like reaction zones, one each on the rich and lean sides of the flow. The simulation and experiment show excellent agreement with respect to the spatial location of the reaction zones.

Combustion proceeds in two distinct separated reaction zones, one an inner premixed flame and the other an outer nonpremixed flame. The two reaction zones in analogous counterflow flames are "merged" due to higher strain rate effects [28]. This is due to flowfield differences between one- and two-dimensional flames, since merged partially premixed flames can be retracted into double flames provided the flowfield stretch rates are low enough [29]. The highest temperatures occur in the outer flame. The chemistry is frozen in the region between the inner and outer reaction zones despite the high temperatures there due to a local scarcity of hydroxyl radicals that are required to oxidize the intermediate species CO and H_2, which are formed in the inner (premixed-like) reaction zone. Based on the heat release rate profiles, the inner and outer flame lengths are, respectively, 16 and 48 mm. Both these heights agree with the measured values obtained from the emission images of Fig. 1b. The reaction and heat release rates are much weaker at the tip of the outer flame than at its base, whereas the inner premixed flame has comparable reaction and heat release rates at both its tip and base.

Figure 2 compares the experimentally obtained and computed velocity vectors in the 1-g flame discussed in the context of Fig. 1b. The flame interface separates smaller velocity magnitudes on the reactant side from larger values on the partially burned side in both sets of data. The measured and predicted results are in excellent agreement. Flow dilatation due to the inner flame heat release causes the velocity vectors to move away from the centerline. The experimental data are sparse in some postflame regions, since dilatation reduces the particle seed densities in those areas considerably. Consequently, there is some discrepancy in the comparison in the postflame region due to experimental uncertainties.
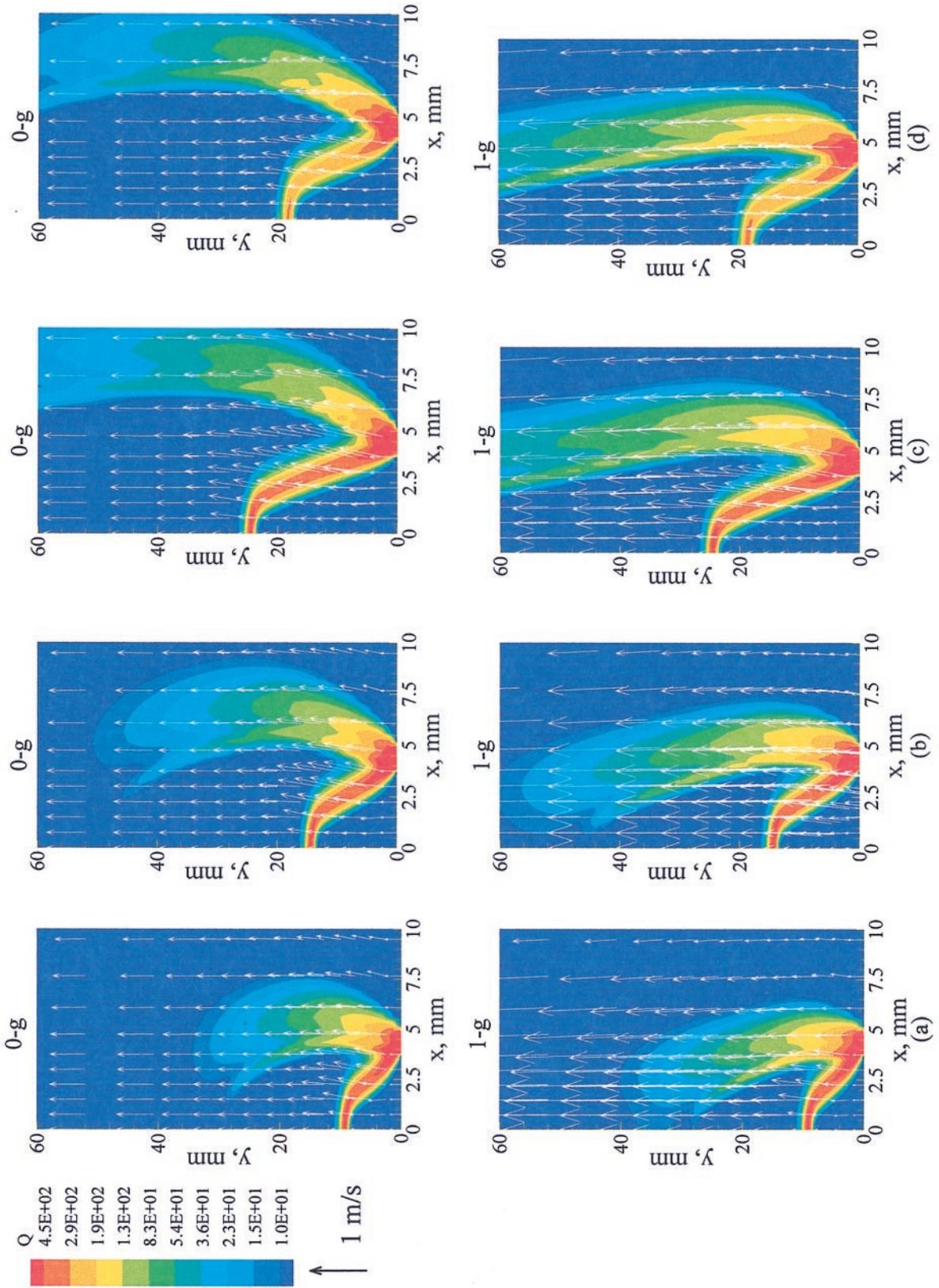
Figure 3 depicts the normal- and zero-gravity flame structures for different values of V_{reac} and ϕ. For both the 1-g and 0-g flames, the inner and outer reaction zone heights increase as either or both of the reactant velocity and the equivalence ratio are increased. The dependence of the inner flame height on the reactant velocity is attributable to the residence time, since the chemical reaction time essentially depends only on the equivalence ratio. Consequently, the premixed reaction zone moves to increasingly higher axial locations as V_{reac} is raised. On the other hand, the chemical reaction time also increases as ϕ is increased and, consequently, the inner flame height increases. The increase in the outer flame height with larger reactant velocities is attributed to two factors: (1) Due to the strong synergistic interactions between the two flames, the outer flame height increases with the inner flame height. (2) Larger values of V_{reac} enhance the advection fluxes of CO and H_2 (that are provided by the inner reaction zone and serve as intermediate fuels) that move the outer flame farther downstream in the axial direction.

We have found that the heights of both the inner and outer reaction zones at 1-g are well-correlated with the function $F = V_{\text{reac}}(1 + V_{\text{reac}}/V_{\text{air}})(\phi - 1)$, where V_{reac} denotes the velocity of the flow issuing from the inner slot, and V_{air} represents the velocity of the air introduced from the outer slot [13]. A linear best fit provides relations for the inner reaction zone height $L_i = (0.3F + 2)$ mm, and the outer height $L_O = (0.6F + 20)$ mm in the ranges

$25 \leq F \leq 280$ mm, $5 \leq L_i \leq 85$ mm, and $20 \leq L_i \leq 145$ mm.

Another important observation from Fig. 3 is that the presence of gravity reduces the spatial separation between the inner and outer reaction zones and, thereby, enhances the interaction between these regions. In addition, while the inner flame characteristics are essentially unaffected by gravity, the outer flame shows a strong sensitivity to gravity. For all the cases considered, the presence of gravity makes the outer flame more compact, taller, and closer to the inner flame. In addition, the outer flames exhibit weaker reaction rates at their tips at zero-gravity as compared to their 1-g counterparts. This is apparently caused by the relatively enhanced diffusive fluxes downstream of the inner premixed zone compared to the reduced advection fluxes in the outer region for the 0-g flames. This may have important implications with regard to the overall pollutant formation in partially premixed flames, especially with respect to CO leakage from the zero-gravity flames.

The iso-temperature contours for two flames, one established at 1 g and the other at 0 g at $\phi = 2$ and $V_{\text{reac}} = V_{\text{air}} = 30$ cm s^{-1}, are presented in Fig. 4. The corresponding heat release rate profiles are contained in Fig. 3b. In the 1-g case the reactants flow out of the burner in an opposite direction to the gravitational vector. The Froude number $\text{Fr}(=V_{\text{reac}}^2/gL = 1.22)$ for the 1-g flame is of order unity so that the inertial and gravitational effects are of similar magnitude. The air entrainment that occurs at 1 g is illustrated by the direction of the velocity vectors in the outer flow that turn toward the centerline. Flow dilatation due to the inner flame heat release causes the velocity vectors to move away from the centerline. The temperature of the outer reaction zones is higher than in the respective inner zones. The heat release rates associated with the two inner (rich-side) reaction zones are similar for the two flames. However, the outer reaction zone heat release rates are different for the two flames, since buoyancy effects elongate the outer nonpremixed flame in the presence of gravity. Consequently, the inner reaction zones exhibit like temperature profiles for the two cases, whereas the outer reaction zone temperatures are dissimilar. Buoyancy effects cause the outer reac-
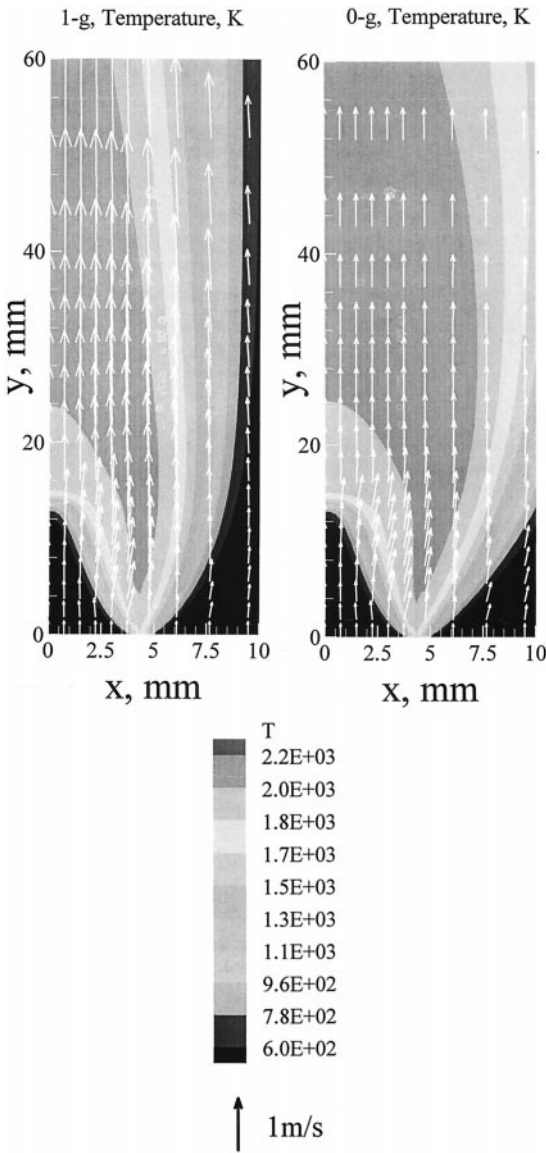
Fig. 4. Temperature profiles for (a) 1-g and (b) 0-g flames, both established at $\phi = 2$ and $V_{\text{reac}} = V_{\text{air}} = 30$ cm s^{-1}.

the presence of gravity, buoyancy effects accelerate the products and, consequently, direct the velocity vectors toward the centerline. Therefore, the advection of the (outer) air flow into the outer reaction zone increases in the presence of gravity. While the inner reaction zone height based on the heat release profile is unaffected by gravitational effects, the topography of the outer reaction zone is significantly different. The 1-g flame exhibits much steeper temperature gradients in its outer reaction zone as the enhanced air advection both increases the local reaction rate and cools that region.

The spatial changes in the outer flame chemistry are illustrated in Fig. 5 which compares the reaction rate contours of the major fuel decomposition reaction $CH_4 + H \Leftrightarrow CH_3 + H_2$ and the product-formation reaction $H_2 + OH \Leftrightarrow H_2O + H$ for the two flames. Whereas the outer reaction zone tip is closed at 1 g (based on the methane-consumption reaction), that for the 0-g flame is open. Likewise, water formation occurs in a broader spatial region at zero gravity. This is due to the relatively limited transport of air into the outer reaction zone under 0-g conditions so that the fuel must diffuse farther into the air stream in order to meet its oxidizer demand. The corresponding inner reaction zones exhibit much smaller topographical differences. The inner zone reaction rate intensity at 0 g is slightly lower. The methane consumption rate is higher in the inner premixed flame due to its higher concentrations in that region. Since oxygen is deficient in the premixed reaction zone, methane leaks through it and is also consumed in the nonpremixed flame, although at lower rates. The outer reaction zone is transport-limited and is, therefore, spatially thicker than the inner premixed flame.

A detailed examination of the reaction rates previously reported by us [11, 13] indicated that: (1) The major pathway for methane consumption proceeds through the reactions $CH_4 + H \Leftrightarrow CH_3 + H_2$, $CH_3 + O \Leftrightarrow CH_2O + H$, $CH_2O + H \Leftrightarrow CHO + H_2$, and $CHO + M \Leftrightarrow$

tion zone to become slender and more compact than in the corresponding 0-g case.

The effects of flow dilatation are apparent along the premixed flame both in the presence and absence of gravity, and gas expansion turns the velocity vectors away from the centerline. In

Fig. 3. Heat release rate contours and velocity vector plots for several normal- and zero-gravity flames (for all of the cases $V_{\text{air}} = 30$ cm/s): (a) $V_{\text{reac}} = 20$ cm/s, $\phi = 2.0$; (b) $V_{\text{reac}} = 30$ cm/s, $\phi = 2.0$; (c) $V_{\text{reac}} = 50$ cm/s, $\phi = 2.0$; (d) $V_{\text{reac}} = 30$ cm/s, $\phi = 2.5$.

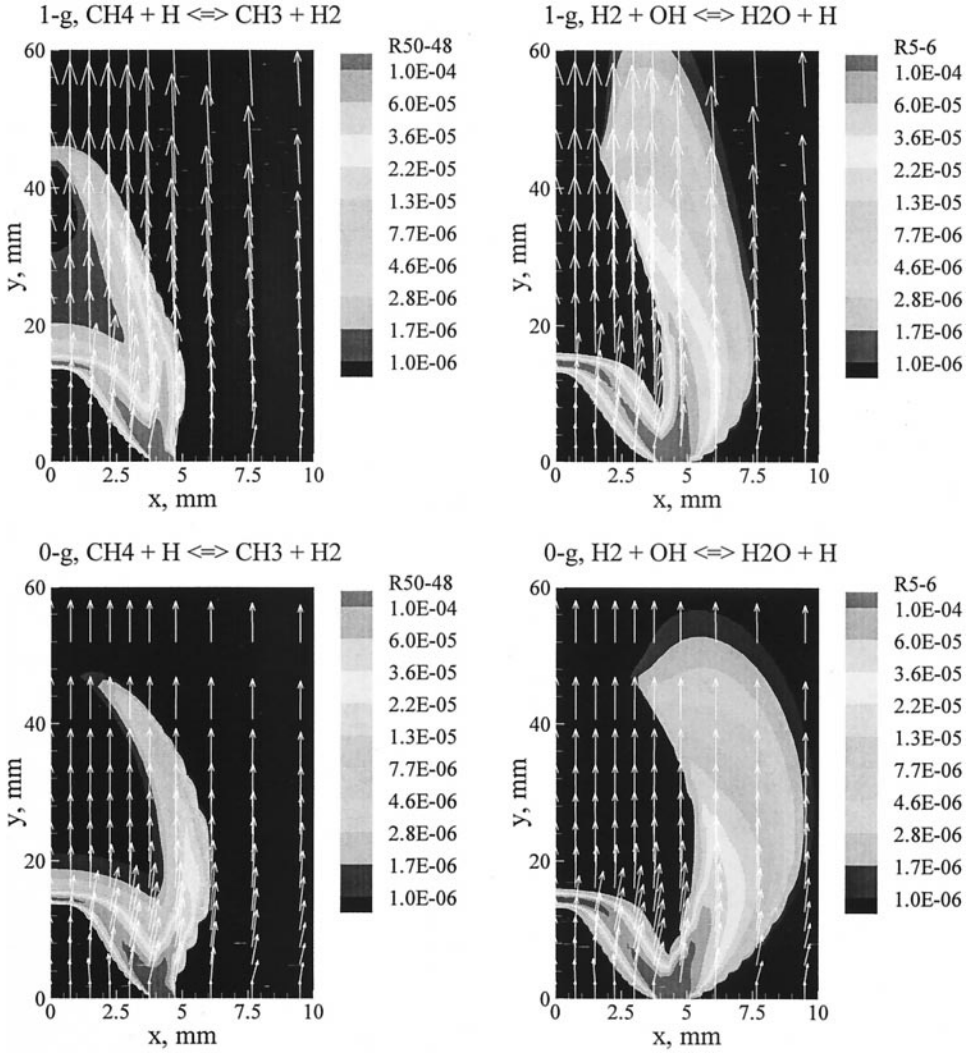Fig. 5. Contours of two major chemical reaction rates $CH_4 + H \Leftrightarrow CH_3 + H_2$ and $H_2 + OH \Leftrightarrow H_2O + H$ for the (a) 1-g and (b) 0-g flame established at $\phi = 2$ and $V_{reac} = V_{air} = 30$ cm s^{-1}.

CO + H + M; (2) Carbon monoxide and hydrogen are oxidized in the outer nonpremixed flame, respectively, through the reactions CO + OH $\Leftrightarrow$ CO$_2$ + H and H$_2$ + OH $\Leftrightarrow$ H$_2$O + H; and (3) O$_2$ is converted into hydroxyl radicals in this flame through the sequential reactions O$_2$+H + M $\Leftrightarrow$ HO$_2$ + M and HO$_2$ + H $\Leftrightarrow$ OH + OH. In those investigations we reported that the two reaction zones are synergistically coupled and each provides heat and/or chemical species for the other. The premixed flame requires H-atoms for the reactions that initiate CH$_4$ and O$_2$ consumption and produces the partial oxidation products CO and H$_2$ (which

provide the fuel for the nonpremixed flame). The nonpremixed flame consumes the premixed flame products and, in turn, produces H-atoms that are, in part, transported back into the inner region [11, 13]. Our results show that the heat release rate profile strongly correlates with CO- and H$_2$-oxidation [13]. Therefore, the region between the inner and outer flames is characterized by heat and mass transport by both advection and diffusion, but where negligible chemical reaction occurs due to the relative paucity of hydroxyl radicals that are required to oxidize CO and H$_2$.

The advection of O$_2$, CH$_4$, and H-atoms in

both the 1- and 0-g flames is illustrated in Fig. 6. The advection term is $\rho u Y_i \vec{i} + \rho u Y_i \vec{j}$, where $\vec{i}$ and $\vec{j}$ denote the directional vectors. The advection of methane and oxygen into the inner reaction zone is very similar for the two flames. Under normal gravity conditions methane is advected toward the centerline at higher axial and radial locations ($y > 20$ mm, $x > 2.5$ mm), while at 0 g this CH_4-transport in this manner is roughly parallel to the centerline. The difference between the two flames is clearer in the context of O_2 advection, since buoyancy both accelerates the flow and greatly enhances oxidizer transport toward the centerline. While the advection of H-atoms in the region of the inner reaction zone is similar for both the 1- and 0-g flames, it is markedly dissimilar in the region of the outer reaction zone. Therefore, buoyant transport enhances radical advection into the outer reaction zone. In contrast, the flux of radical species into the outer reaction zone of the zero-gravity flame is smaller and, consequently, the reactant residence times are larger in the outer zone of that flame. The advective flux of the various species in the region contained between the inner and outer reaction zones is much larger at normal gravity and, consequently, the separation between the inner and outer reaction zones is smaller at 1-g. In general, buoyancy effects increase the advection of all species. The consequence of this is that the 1-g flames exhibit larger emission of unburned intermediates, such as CO and H_2 (as discussed later in context of Figs. 11a and b).

In summary, the zero-gravity flame is spatially broader than the normal gravity flame. While the inner premixed spatial region appears to be relatively unaffected by gravitational effects, the outer flame is significantly dissimilar for the two cases. The gravitational effects that occur in the postflame zone of the inner flame do not significantly influence its upstream region in accord with previous results for premixed flames [30]. The reactions along the carbon-consumption chain are weaker in the outer nonpremixed region at zero-gravity and occur in a larger reaction volume. The outer flame is thicker in the absence of gravity, since buoyant mixing is absent, suggesting that its structure will be more sensitive to any flow or stoichiometry perturbations.

The diffusive flux, which has the form $-(\rho D_{i-N_2})(\partial Y_i/\partial x)\vec{i} + (\rho D_{i-N_2})(\partial Y_i/\partial y)_i\vec{j}$, of O_2, CO, and OH radicals for the two flames is compared in Fig. 7. Buoyancy effects have a negligible impact on the diffusion of species into and out of the inner reaction zone. The diffusive fluxes associated with the outer reaction zone are, however, influenced by gravity, since that reaction zone topography, and, therefore, the species concentration gradients are different in the two flames. The enhanced mixing in the outer reaction zone at 1 g causes the reactions to proceed faster and the oxygen gradients to be steeper. This also increases oxygen diffusion into that region under normal gravity. The slower oxygen transport at 0 g induces the carbon monoxide to diffuse further away from the centerline before its conversion into CO_2 by hydroxyl radicals. Overall, gravity does not impact the diffusive fluxes as strongly as it does advection, in particular, in the outer reaction zone. However, the relative influence of the diffusive fluxes in comparison to advection is significantly enhanced in the absence of gravity.

Flame stretch occurs due to both flow non-uniformities along the flame surface and curvature [31]. The outer flame exhibits a larger curvature (based on either the heat release or various reaction rates) in the absence of gravity (cf. Fig. 3). The normal gravity outer flame is curved at its base and virtually planar elsewhere. The tips of both the inner and outer reaction zones appear to be locally planar (based on the local advection) so that the local stretch rate there is essentially due to aerodynamic straining alone. While the flow is oblique to the inner reaction zone surface everywhere, it is virtually normal to the outer flame surface in the vicinity of the centerline. Therefore, the inner reaction zone is stretched at the centerline, whereas the outer flame experiences negligible stretch. The fuel-side strain rate (in this case that associated with the inner flame) has been previously interpreted as a sensitive indicator of partially premixed flame structure in one-dimensional counterflow flames [28]. Figure 8a presents the centerline velocity profiles for several flames, which show large differences due to gravitational effects. The velocity profiles prior to the inner flame are nearly identical in the presence and absence of gravity, but exhibit significant
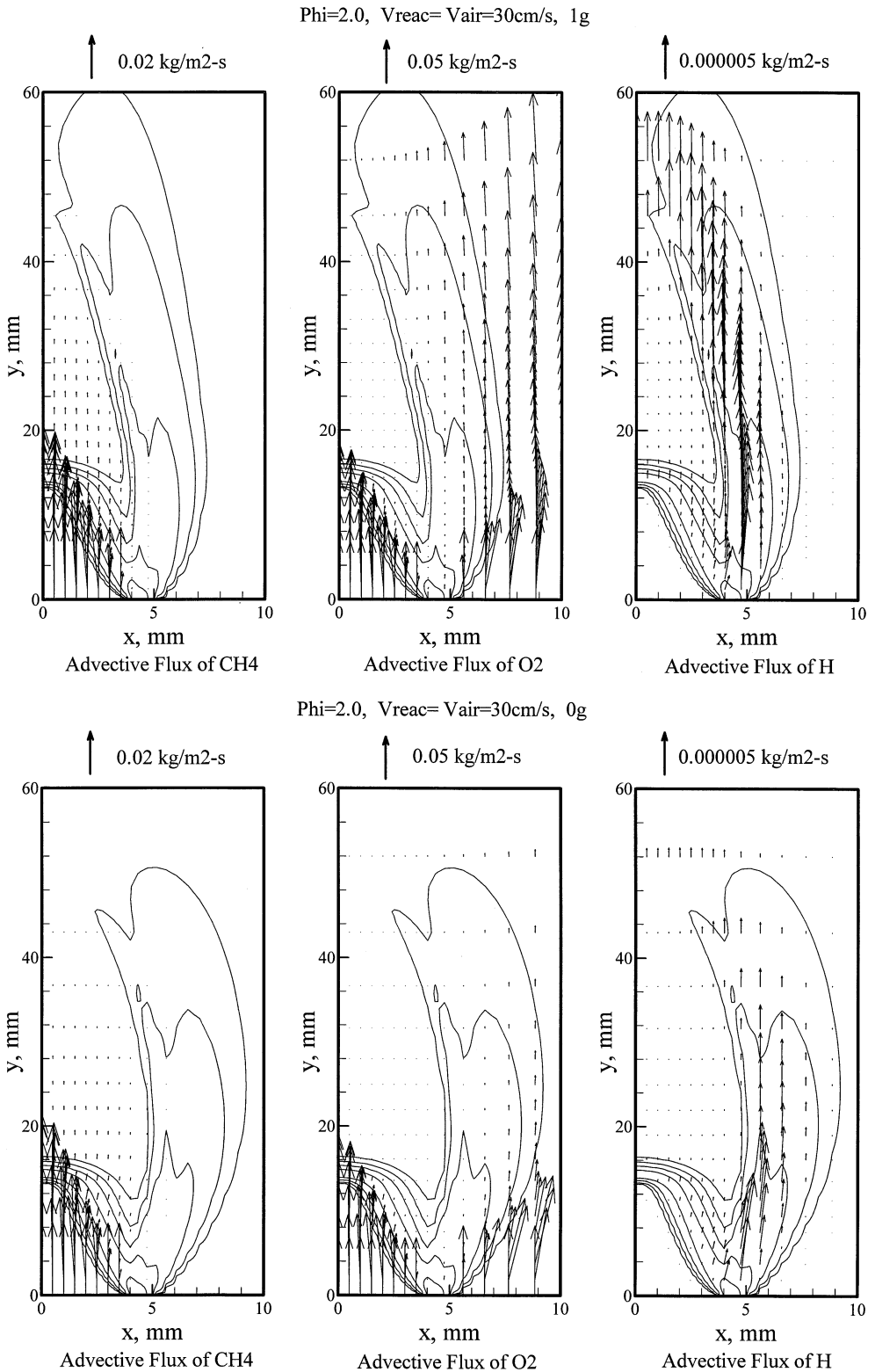
Phi=2.0, Vreac= Vair=30cm/s, 1g

0.02 kg/m2-s   0.05 kg/m2-s   0.000005 kg/m2-s

Advective Flux of CH4   Advective Flux of O2   Advective Flux of H

Phi=2.0, Vreac= Vair=30cm/s, 0g

0.02 kg/m2-s   0.05 kg/m2-s   0.000005 kg/m2-s

Advective Flux of CH4   Advective Flux of O2   Advective Flux of H

Fig. 6. Advection flux of CH_4, O_2, and H-atoms under (a) normal-gravity and (b) zero-gravity conditions. A scale for the magnitude of the vectors is provided at the top of the figures.
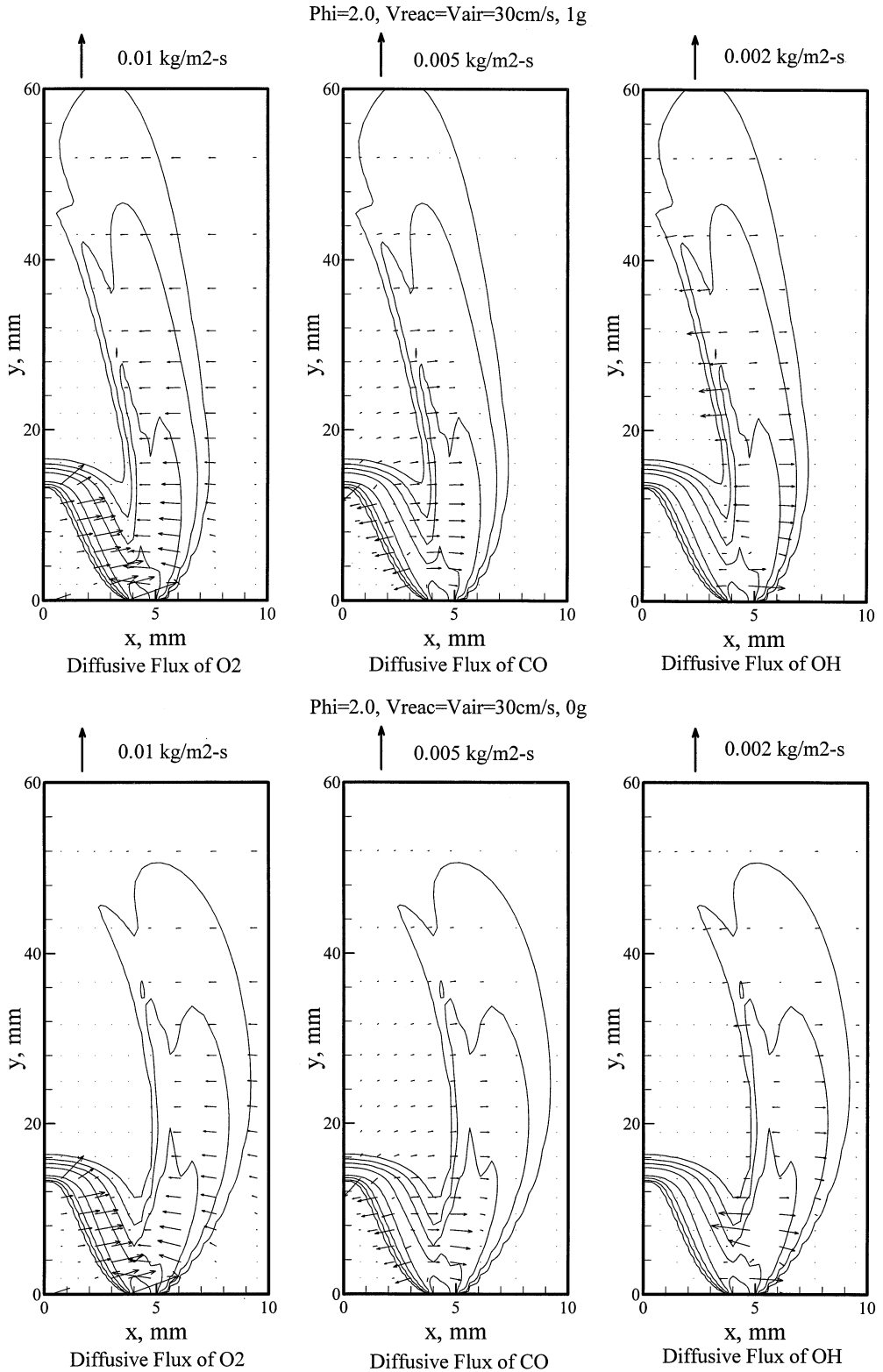
Phi=2.0, Vreac=Vair=30cm/s, 1g

0.01 kg/m2-s   0.005 kg/m2-s   0.002 kg/m2-s

Diffusive Flux of O2   Diffusive Flux of CO   Diffusive Flux of OH

Phi=2.0, Vreac=Vair=30cm/s, 0g

0.01 kg/m2-s   0.005 kg/m2-s   0.002 kg/m2-s

Diffusive Flux of O2   Diffusive Flux of CO   Diffusive Flux of OH

Fig. 7. Diffusion flux of O_2, CO, and OH radicals under (a) normal-gravity and (b) zero-gravity conditions. A scale for the magnitude of the vectors is provided at the top of the figures.
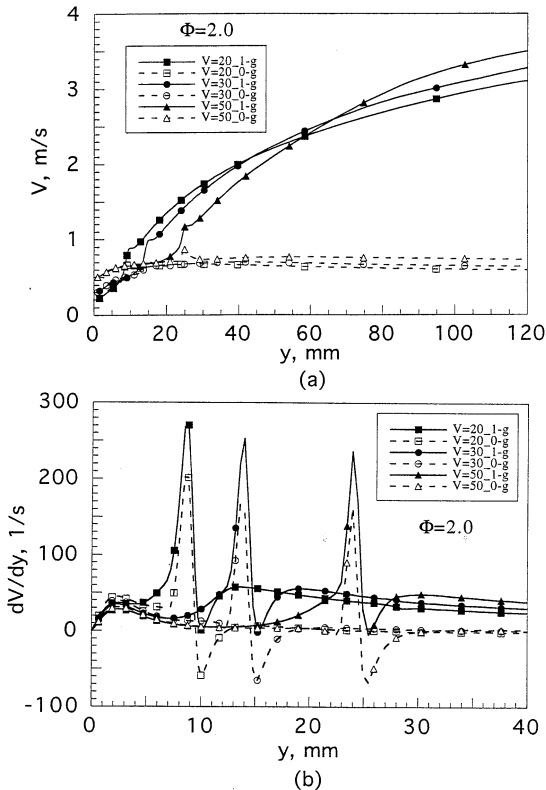
Fig. 8. Profiles of centerline (a) velocity, and (b) strain rate for normal- and zero-gravity flames established at $\phi = 2$, $V_{air} = 30$ cm s^{-1}, and $V_{reac} = 20$, 30, and 50 cm s^{-1}.

differences in the postflame region. The zero-gravity flames exhibit a small velocity increase due to dilatation, whereas the velocity in the normal-gravity flames increases severalfold due to buoyancy effects.

Since there are no transverse gradients or transverse velocity components along the centerline, the strain rate tensor there contains a single component, i.e., the normal axial strain rate. The corresponding centerline normal strain rates for the flames discussed in Fig. 8a are presented in Fig. 8b. These rates vary, having their largest and smallest values, respectively, in the preheat and the heat release regions of the inner reaction zone. The normal strain rate in the initial cold flow is unaffected by gravity. Just prior to the preheat zone, the normal strain rate is negligible when $V_{reac} = 30$ and 50 cm s^{-1}. Therefore, the double flame structure (that is not apparent at this stoichiometry in higher shear strain rate counterflow

flames [28]) is due to the lower strain rates in the two-dimensional configuration. Increasing the initial reactant velocity decreases the maximum values of the normal strain rate. Further downstream, the rates relax to moderate values under normal-gravity conditions, and are negligible in the absence of gravity. In general, the absence of gravity decreases the local strain rate allowing for further spatial separation of the two reaction zones.

The spatial broadening of the reaction zone due to gravity is illustrated in Figs. 9a–c which present various spatially integrated (in the axial direction) reaction rate profiles with respect to transverse position. Figure 9a presents the transverse profile of the spatially integrated methane consumption reaction for the two flames. While the reaction is concentrated around one axial location at 1 g, since the outer flame is wider at 0 g, the reaction proceeds at two distinct axial locations at that condition. This is also true of the CO- and H_2-oxidation reactions as illustrated in Figs. 9b and c. The reactions peak in the vicinity of the axial location of the flame base at both normal- and zero-gravity. At 0 g, the reaction rates also exhibit peaks at transverse locations that are further displaced from the centerline. The increased spatial separation between the inner and outer reaction zones at 0 g is also evident from Figs. 9a–c.

In contrast, if the reaction rates are spatially integrated in the transverse direction, their normal- and zero-gravity profiles are similar for the two flames. This is illustrated in Fig. 9d through the profile of the reaction $H_2 + OH \Leftrightarrow H_2O + H$. Although the transversely integrated reaction rate is slightly higher at higher axial locations for the 1-g flame, the (axial) differences between the two flames are not as pronounced as in the transverse direction (cf. Figs. 9a–c). These figures again illustrate how the outer nonpremixed-type reaction zone must move outward into the air stream to meet the oxidizer demand of the unburned methane and the intermediate species CO and H_2.

The effects of varying strain rates, and multi-dimensional transport of heat and radicals on the flame structure can be investigated by examining the state relationships of the various scalars. Previous investigations have found that
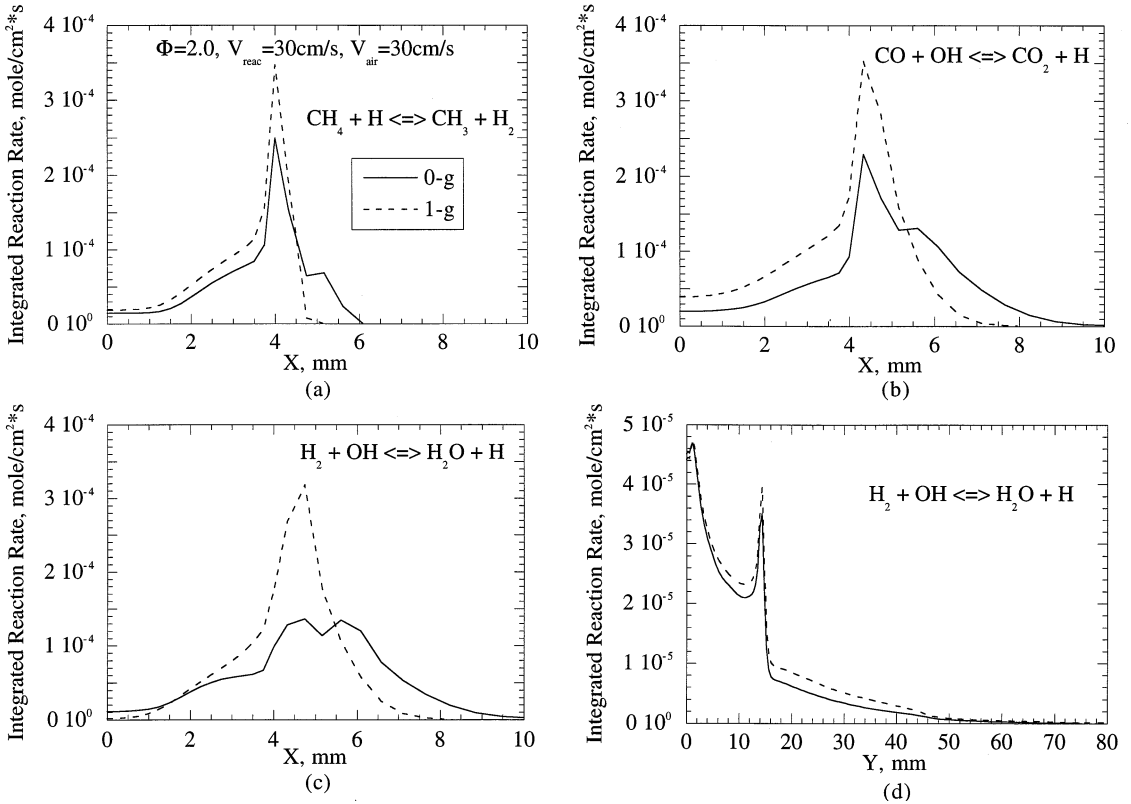
Fig. 9. Integrated rate profiles with respect to the transverse direction for the reactions (a) $CH_4 + H \Leftrightarrow CH_3 + H_2$; (b) $CO + OH \Leftrightarrow CO_2 + H$; (c) $H_2 + OH \Leftrightarrow H_2O + H$; and (d) (with respect to the axial direction) for the reaction $H_2 + OH \Leftrightarrow H_2O + H$.

state relationships (in terms of the mixture fraction) for the major species are generally applicable to nonpremixed hydrocarbon–air flames established in various configurations over a range of strain rates [32]. It is known that partially premixed flames can also be characterized with respect to a modified mixture fraction $\xi = (Z - Z_l)/(Z_r - Z_l)$, where Z denotes the relative local mass fraction originating in the fuel, and the subscripts r and l are conditions relevant at the boundaries of the rich and lean regions, respectively [1, 3, 8, 11].

State relationships for the temperature and H_2 mass fraction are presented in Fig. 10 along three sets of transverse locations with respect to ξ (defined in terms of the local nitrogen mass fraction) for two flames established under similar flow and stoichiometric conditions, but under normal- and zero-gravity. The temperature and H_2 profiles clearly show the two rich- and lean-side reaction zones. The lean-side temper-

ature is higher, as has been previously noted [28, 29]. The locations of both the rich and lean reaction zones differ with respect to ξ, depending on their transverse positions. Due to the spatial differences between the 0- and 1-g flames on the lean side we expect the state relationships to differ in that region. The peak temperature on the lean side is 2181 K for the 0-g flame and 2164 K for the 1-g flame. This small reduction in the peak temperature can be explained by the enhanced mixing of fuel and air in the presence of gravity and the buoyancy-induced convective heat transfer.

The inner (rich-side) reaction zone shifts towards less-rich locations in the presence of gravity as seen from the profiles contained in Fig. 10. It is clear from Fig. 6 that the flow divergence is larger as one moves transversely outward from the centerline, and consequently, the local strain rate also increases. The two-dimensional slot flame is characterized by a
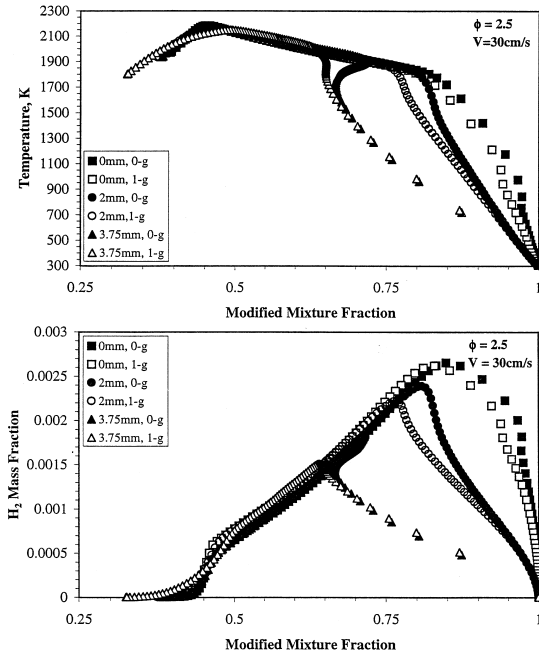
Fig. 10. Profiles of axial (a) temperature, and (b) H_2 mass fraction with respect to the modified mixture fraction for normal- and zero-gravity flames established at $\phi = 2.5$, $V_{air} = V_{reac} = 30$ cm s^{-1} along three transverse locations: $x = 0$, 2, and 3.75 mm.
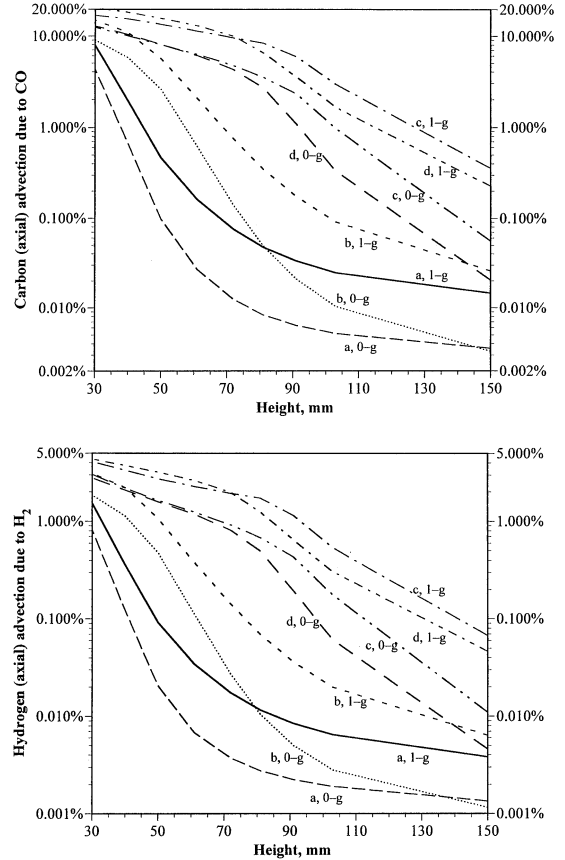

Fig. 11. The axial advection of (a) carbon contained in CO, and (b) hydrogen contained in H_2 as a weight percentage of both species introduced into the domain in the form of CH_4. The conditions a, b, c, and d are the same as for the normal- and zero-gravity flames discussed in the context of Fig. 3.

multiplicity of local aerodynamic strain rates. The results contained in Fig. 10 show that as the local strain rate increases, the inner rich-side reaction zone moves closer in mixture fraction space to the lean outer reaction zone. Consequently, while gravity affects the outer lean reaction zone, strain rate effects are more pronounced on the inner reaction zone. Since the presence of gravity slightly increases the strain rate experienced by the rich inner reaction zone, its location in the 1-g flame moves relatively closer to the lean side in mixture fraction space as compared to the 0-g flame. In accord with a residence time criterion, the H_2 mass fraction in the outer reaction zone decreases with increasing flame straining.

Figures 11a and b, respectively, present the fractional axial advection of carbon atoms (contained in CO) and hydrogen atoms (contained in H_2) in comparison to their flux in the form of fuel. The fractional axial advection of either elemental species is calculated through the expression $(a_{k,i}/a_{k,\mathrm{CH_4}})(W_{\mathrm{CH_4}} \int_0^L Y_i \rho v_y \, dx)/(W_i \int_0^L (Y_{\mathrm{CH_4}} \rho v_y)_0 \, dx)$, where W denotes the mo-

lecular weight, Y the mass fraction, ρ the density, v_y the axial velocity, L the width of the computational half domain, the subscript i refers to either CO or H_2, while the subscript 0 refers to conditions at the influx plane into the domain, i.e., at $y = 0$ which is the burner exit. The ratio $(a_{k,i}/a_{k,\mathrm{CH_4}})$ refers to the relative number of atoms of element k (either C or H) contained in species i (respectively, CO or H_2) compared to the corresponding number in CH_4. The carbon and hydrogen fractional advection is presented in Figs. 11a and b for the eight flames that are discussed in the context of Fig. 3. In general, the fractional advection of these elemental species is always greater at 1 g, confirming the relatively enhanced role of molecular transport in the absence of gravity. The simulations show that the value of the fractional

advection rises when either V_{react} or the inner equivalence ratio is increased.

The introduction of buoyancy increases the unburned carbon and hydrogen loss from the domain, since the higher advection under normal gravity reduces the residence time available for complete combustion of the intermediate fuels CO and H_2. Therefore, at 1 g the percentage of carbon advection at a 150 mm height approximately varies between 0.01% (for the V_{air} = 30 cm/s, V_{reac} = 20 cm/s, ϕ = 2.0 flame) to 0.4% (for the V_{air} = 30 cm/s, V_{reac} = 50 cm/s, ϕ = 2.0 flame). The corresponding range for the zero-gravity flames is lower by almost one order of magnitude, lying between 0.003–0.06%. The analogous bounds for the fractional unburned H-atom loss lies between approximately 0.004–0.07% for the 1-g flames, and between 0.001–0.01% for the 0-g flames. The 1-g flames have more vigorous reaction at the tips of the outer nonpremixed reaction zone which tends to decrease the unburned C- and H-atom losses. However, the enhanced advection in the presence of gravity dominates and, consequently, leads to higher CO and H_2 emissions than at 0 g.

Finally, we address the issue of thermal radiation. The radiative cooling time τ_r for a gaseous volume initially at the adiabatic flame temperature T_f can be estimated as $\tau_r = T_f/(dT/dt) \approx T_f/(q/\rho c_p)$, where q denotes the heat loss rate, ρ the density, and c_p the constant pressure specific heat [33]. Using the optically thin gas assumption, $q = [4\sigma a_p(T_f^4 - T_O^4)]$ (where σ represents the Stefan-Boltzmann constant, a_p the Planck mean absorption coefficient, and T_O the ambient temperature) and the ideal gas state relationship, τ_r can be expressed in the form $\tau_r \approx \{\gamma/(\gamma - 1)\}P/\{4\sigma a_p(T_f^4 - T_O^4)\}$, where γ denotes the specific heat ratio, and P the ambient pressure. Assuming atmospheric conditions, $a_p = 56$ cm^{-1}, $\gamma = 1.35$, $T_O = 298$ K, and the "flame" temperatures in typical methane–air partially premixed flames to vary from 1650 K in the inner premixed reaction zone to 2200 K in the outer nonpremixed region, the corresponding τ_r values lie in the range 0.3–0.09 s.

The diffusive time scale $\tau_d = \delta^2/\alpha$ represents the molecular transport of species or thermal energy across a region of thickness δ, with α denoting a temperature-averaged (mass or thermal) diffusivity. The buoyant transport time scale $\tau_b \approx L/U_b$. Here, L represents a characteristic length, and $U_b \approx [gL(\Delta\rho/\rho)]^{1/2}$ is the buoyancy-induced velocity, with g denoting the gravitational acceleration, ρ density, and $\Delta\rho$ the density change across the flamefront. For flames $\Delta\rho/\rho \approx 1$ with the result that $\tau_b \approx (L/g)^{1/2}$ [33].

We assume representative values for α and g, respectively equal to 1.5 cm^2 s^{-1} and 980 cm s^{-2} [33]. For typical characteristic length scales in the range 1–10 cm, τ_b varies from 0.03–0.1 s. For τ_d to lie within these bounds, the transport region must be 2 to 4 mm thick. This thickness depends on the level of partial premixing and the velocities of the reactant streams. Therefore, if the transport zone thickness exceeds 4 mm (as is the norm in the slot burner flames that we have investigated), gravitational effects overwhelm transport effects, since $\tau_b < \tau_d$. This is clearly illustrated in the comparisons between 1- and 0-g flames contained in Figs. 3–7.

For typical characteristic length scales in the range 1–10 cm, τ_b varies from 0.03–0.1 s. Hence, radiation effects may be relatively unimportant at normal gravity, since buoyant convection is a faster process. On the contrary, under microgravity conditions at which τ_b is sufficiently large, radiation effects are expected to be more significant. Therefore, future studies should address the issue of thermal radiation from these flames, particularly since heat losses should further weaken the 0-g outer reaction zone tip.

CONCLUSIONS

We have presented the results of a numerical investigation of two-dimensional partially premixed methane–air flames established under both normal- and zero-gravity. The computational model has been previously validated. Further validation is obtained by comparing the experimentally obtained chemiluminescent emission due to excited-C_2^* free radical species with the simulated heat release for a representative flame.

1. The structure of a near-unity Froude number flame is discussed. Combustion occurs in two reaction zones, one an inner premixed flame

and the other an outer nonpremixed flame. The reaction and heat release rates are much weaker at the tip of the outer flame than at its base. The inner premixed flame has comparable reaction and heat release rates at both its tip and base.

2. The premixed flame requires H-atoms for CH_4 and O_2 consumption, and produces CO and H_2 (which provide the "fuel" for the nonpremixed flame). The nonpremixed flame consumes these products and, in turn, produces H-atoms that are transported back into the inner region.

3. The zero-gravity flame is spatially larger than the corresponding normal-gravity flame. While the spatial characteristics of the inner premixed region are relatively unaffected by gravitational effects, the outer nonpremixed zones exhibit significant differences. More air is advected into the outer reaction zone in the presence of gravity. Consequently, the outer flame is thicker for the 0-g case, since the role of radial diffusive transport is relatively enhanced. While buoyancy effects significantly influence advection, gravity has a small effect on the absolute values of the species' diffusive fluxes.

4. The inner reaction zone is strained at the centerline, whereas the outer zone experiences negligible strain and this lower strain rate allows a double-flame structure to exist. The absence of gravity decreases the local value of the normal strain rate allowing for further spatial separation of the two reaction zones.

5. The presence of gravity reduces the spatial separation (and thereby enhances the interactions) between the inner and outer reaction zones. The outer reaction zones are more compact, taller, and exhibit more vigorous reaction at their tips at 1-g than at zero-gravity.

6. The presence of buoyancy significantly influences the region downstream of the inner reaction zone. Consequently, the inner (rich-side) reaction zone shifts slightly toward less-rich locations in the presence of gravity. The two-dimensional flame is characterized by a multiplicity of local aerodynamic strain rates. As this rate increases, the inner rich-side reaction zone moves closer in mixture fraction space to the lean outer reaction zone.

7. Buoyancy effects increase the advection, thereby reducing the residence time available for the oxidation of CO and H_2. Consequently, there is a larger loss of unburned C- and H-atoms from the 1-g flames than in the absence of gravity. Although the 1-g flames involve more vigorous reaction at their tips (which would decrease the unburned C- and H-atom losses), the enhanced advection dominates and leads to higher CO and H_2 emissions than at zero-gravity.

REFERENCES

1. Peters, N., *Twentieth Symposium (International) on Combustion*, The Combustion Institute, Pittsburgh, 1984, pp. 353–360.
2. Smooke, M. D., Seshadri, K., and Puri, I. K., *Twenty-Second Symposium (International) on Combustion*, The Combustion Institute, Pittsburgh, 1988, pp. 1555–1563.
3. Rogg, B., Behrendt, F., and Warnatz, J., *Twenty-First Symposium (International) on Combustion*, The Combustion Institute, Pittsburgh, 1986, p. 1533.
4. Yamaoka, I., and Tsuji, H. *Fifteenth Symposium (International) on Combustion*, The Combustion Institute, Pittsburgh, 1974, p. 737.
5. Yamaoka, I., and Tsuji, H. *Sixteenth Symposium (International) on Combustion*, The Combustion Institute, Pittsburgh, 1976, p. 1145.
6. Yamaoka, I., and Tsuji, H. *Seventeenth Symposium (International) on Combustion*, The Combustion Institute, Pittsburgh, 1978, p. 843.
7. Hamins, A., Thridandam, H., and Seshadri, K., *Chem. Eng. Sci.* 40:2027–2038 (1985).
8. Seshadri, K., Puri, I., and Peters, N., *Combust. Flame* 61:237–249 (1985).
9. Law, C. K., Li, T. X., Chung, S. H., Kim, J. S., and Zhu, D. L., *Combust. Sci. Technol.* 64:199–232 (1989).
10. Shu, Z., Aggarwal, S. K., Katta, V. R., and Puri, I. K., *Combust. Flame* 111:276–295 (1997).
11. Shu, Z., Aggarwal, S. K., Katta, V. R., and Puri, I. K., *Combust. Flame* 111:296–311 (1997).
12. Yule, A. J., Chigier, N. A., Ralph, S., Boulderstone, R., and Ventura, J., *AIAA J.* 19:752–760 (1981).
13. Shu, Z., Krass, B. J., Choi, C. W., Aggarwal, S. K., Katta, V. R., and Puri, I. K., *Twenty-Seventh Symposium (International) on Combustion*, Boulder, Colorado, August 2–7, 1998, Paper No. 049 (accepted).
14. Kee, R. J., Miller, J. A., and Warnatz, J. (1983). *A Fortran Program Package for the Evaluation of Gas-phase Viscosities, Conductivities, and Diffusion Coeffi-*

cients. Rept. SAND83-8209, Sandia National Laboratories.

15. Leonard, B. P., *Comput. Methods Appl. Mechanics Eng.* 19:59–98 (1979).

16. Spalding, D. B., *Int. J. Num. Meth. Mech. Eng.* 4:551 (1972).

17. Katta, V. R., Goss, L. P., and Roquemore, W. M., *Combust. Flame* 96:60–74 (1994).

18. Takahashi, F., and Katta, V. R., *AIAA J. Propulsion Power* 11 (1995).

19. Aggarwal, S. K., Park, T. W., and Katta, V. R., *Combust. Sci. Technol.* 113:429–438 (1996).

20. Patadia, H. (1995). M.S. thesis, University of Illinois at Chicago.

21. Peters, N., in *Reduced Kinetic Mechanisms for Applications in Combustion Systems, Lecture Notes in Physics* (N. Peters and B. Rogg, Eds.), Springer-Verlag, Vol. 15, 1993, pp. 3–14.

22. Pearse, R. W. B., and Gaydon, A. G., *The Identification of Molecular Spectra*, 4th ed., Chapman and Hall, London, 1976, p. 83.

23. Beyler, C. L., and Gouldin, F. C., *Eighteenth Symposium (International) on Combustion*, The Combustion Institute, Pittsburgh, 1981, pp. 1011–1019.

24. Dibble, R. W., Long, M. B., and Masri, A., *Prog. Astronaut. Aeronaut.* 105:99–109 (1986).

25. Brandon, Y., and Samaniego, J.-M., *Combust. Sci. Technol.* 84:81–89 (1992).

26. McManus, K., Yip, B., and Candel, S., *Exptl. Thermal Fluid Sci.* 10:486–502 (1995).

27. Najm, H. N., Paul, P. H., Mueller, C. J., and Wyckoff, P. S., *Combust. Flame* 113:312–332 (1998).

28. Tanoff, M., Smooke, M. D., Osborne, R. J., Brown, T. M., and Pitz, R. W., *Twenty-Sixth Symposium (International) on Combustion*, The Combustion Institute, Pittsburgh, 1996, pp. 1121–1128.

29. Nishioka, M., Nakagawa, S., Ishikawa, Y., and Takeno, T., *Combust. Flame* 98:127–138 (1994).

30. Durox, D., Yuan, T., Baillot, F., and Most, J. M., *Combust. Flame* 102:501–511 (1995).

31. Law, C. K., *Twenty-Second Symposium (International) on Combustion*, The Combustion Institute, Pittsburgh, 1988, pp. 1381–1402.

32. Sivathanu, Y. R., and Faeth, G. M., *Combust. Flame* 82:211–230 (1990).

33. Ronney, P. D., "Combustion Experiments in Space," paper presented at 36th Israel Annual Conference on Aerosciences, Feb. 1996.